

# Stability of a Bose condensed mixture on a bubble trap

Alex Andriati<sup>1,\*</sup>, Leonardo Brito<sup>1,†</sup>, Lauro Tomio<sup>2,‡</sup> and Arnaldo Gammal<sup>1,§</sup>

<sup>1</sup>*Instituto de Física, Universidade de São Paulo, 05508-090 São Paulo, Brazil.*

<sup>2</sup>*Instituto de Física Teórica, Universidade Estadual Paulista, 01156-970 São Paulo, SP, Brazil.*

(Dated: September 21, 2021)

Stability and dynamical behavior of binary Bose-Einstein condensed mixtures trapped on the surface of a rigid spherical shell are investigated in the mean-field level, exploring the miscibility with and without vortex charges, considering repulsive and attractive interactions. In order to compute the critical points for the stability, we follow the Bogoliubov-de Gennes method for the analysis of perturbed solutions, with the constraint that initially the stationary states are in a complete miscible configuration. For the perturbed equal density mixture, of a homogeneous uniform gas and when hidden vorticity is verified, with the species having opposite azimuthal circulation, we consider small perturbation analysis for each unstable mode, providing a complete diagram with the intra- and inter-species interaction role on the stability of the miscible system. Finally, beyond small perturbation analysis, we explore the dynamics of some repulsive and attractive inter-species states by full numerical solutions of the time-dependent Gross-Pitaevskii equation.

## I. INTRODUCTION

The reports on the realization of the long-time predicted Bose-Einstein condensation [1, 2], with ultra-cold repulsive [3, 4] and attractive interacting atoms [5], followed by the possibilities to control the atomic interactions via Feshbach resonance mechanisms [6] (reported in Refs. [7–9]), have opened the door to laboratory investigations to probe plenty of quantum phenomena expected to happen close to zero temperature. Concerning the experimental and theoretical progress on studies with ultra-cold gases, some review papers and textbooks [10–15] are available, providing a broad perspective of the theme, from which other relevant works can be traced.

Just after the first cold-atom experiments, following a theoretical prediction in Ref. [16], two overlapping condensates with spin states of <sup>87</sup>Rb was produced in Ref. [17], with the separation dynamics of the two-spin components of the mixture reported in Ref. [18]. At this time, the properties of binary condensed mixtures having been also investigated in Ref. [19, 20]. Later on, with cold-atom mixtures, we can verify an original theoretical study on rotating properties of two cold-atom species in Ref. [21], which followed by suggestions of possible realizations of ferro-fluidity with two-component dipolar systems [22]. These investigations with binary atomic species became relevant as facing new challenges due to quantum degeneracy for different kinds of atoms, including fermionic isotopes, mixtures of Bose condensates, superfluidity, and Josephson tunneling, as pointed out in Ref. [15]. Some experimental realizations with cold-atom mixtures, as the ones reported in Refs. [23, 24], have provided realistic basis for heteronuclear ultra-cold chemistry, which emerged as a new field of interest with intense

research activities in recent years (see, e.g., Refs. [25–27] and quoted citations).

Relevant in these cases with binary systems are the miscible and immiscible properties, which are derived from relations between the atoms inter- and intra-species two-body interactions [19, 20], and also controlled by the confinement [28, 29]. The control in experimental realizations with different atomic species can be followed by the laboratory activities with ultra-cold molecular systems, as verified for example in Refs. [23, 24, 30–33]. Specifically, in Ref. [31], the dual species with <sup>87</sup>Rb and <sup>41</sup>K were confined in an optical dipole trap in the proximity of inter-species Feshbach resonances. This system was also recently reported in Ref. [34] with attractive interactions. There is also an increasing interest on investigating superfluid mixtures of condensates, which can be experimentally probed as reported in Ref. [35].

Among the studies with dipolar bosonic quantum gases [36–39], motivated by quantum ferrofluid instability observation [40], roton instability and droplet formation with dipole-dipole interaction were investigated in Refs. [41], by solving cubic-quintic Gross-Pitaevskii (GP) formalism [42, 43], where it was pointed out the significant role of three-body interaction in the droplet formations. Later on, the miscibility properties of two-component BECs were investigated in a few works by some of us [44–46], using two different dipolar and non-dipolar hyperfine spin states of a single isotope. These studies were followed by considering mass-imbalance and rotating effects with different isotopes or atomic species in Ref. [47]. Moreover, the studies with dipolar systems presented in Ref. [48] are of particular interest for possible experimental realizations, in which the dipolar interactions are shown to be instrumental to control and tune the interactions of rotating binary mixtures, as well as for the spatial separation of the species. Within a Bogoliubov-de Gennes (BdG) calculation, by exploring possible photonic and rotonic phase transitions, it was pointed out in Ref. [49] the relevance of the confinement geometry, in a work considering the miscibility and sta-

\* andriati@if.usp.br

† brito@if.usp.br

‡ lauro.tomio@unesp.br

§ gammal@if.usp.br

bility of dipolar bosonic mixtures.

The dynamics of binary condensates have also shown remarkable effects in rotating systems [50]. The activities in this direction have been intensified by investigations in which the stability of a system can be probed by considering orbital angular momentum analysis. Among other works, we can mention a miscibility analysis that was performed in Ref. [51], for a binary condensed system in a ring geometry; in Ref. [52], the authors reported a study with repulsive Bose-Einstein condensates (BECs) trapped in a two coupled rings configuration. The Ref. [53] is another recently reported work considering processes in rotating BECs with angular quantum momentum and torque transfer. These kind of investigation with coupled systems are of interest due to the actual experimental possibilities with tunable two-species coupled systems [54–58], which could be applied to condensates confined in spherical geometries by simulating micro-gravity conditions.

On the properties of coherent matter-wave bubbles, the interest started with the investigations reported in Refs. [59, 60], in which one can find a proposal of possible experimental schemes. Recent realistic possibilities in performing cold-atom experiments with low-gravity conditions at the international space station (ISS) [61–63] have drawn particular attention to the studies of condensates confined in bubble traps, as exemplified by Refs. [64–69]. More recently, following observations aboard the international space station with ultracold atom bubbles created by using radio-frequency [70], it was further reported investigations on the nature and properties of bubble configurations with different sizes in Ref. [71]. Among other future experiments in microgravity conditions, it was pointed out in this reference the real perspectives to generate vortices in condensate bubbles through distinct mechanisms, as direct stirring, trap rotation, or spontaneous generation across the condensate phase transition. In view of such advances in the control of condensed bubble generations at the ISS, it seems plausible to believe that further experimental control can be reached in order to tune interacting binary condensed mixtures. With bubble-trapped condensates, we can also point out the recent studies performed in Refs. [72, 73], related to singly quantized vortices and superfluidity.

By considering repulsive Bose-Bose mixtures, following a previous suggestion in Ref. [74], it was recently predicted in Ref. [75] a mixed-bubble regime in which bubbles of the mixed phase coexist with a pure phase of one of the components. Such an interesting study in which self-bound droplets are stabilized by the repulsive Lee-Huang-Yang (LHY) [76] energy contribution, has been also verified in a recent experimental realization, as reported in Ref. [77]. This is a beyond-mean-field effect that occurs for unequal masses or unequal intra-species coupling constants, being due to a competition between the mean-field term, quadratic in densities, and a non-quadratic beyond-mean-field correction (For a related review, with updated bibliography, see Ref. [78]). How-

ever, our following approach still relies on the mean-field GP formalism. We do not consider here the possibility of canceling the two-body interactions and consequent overvaluing the LHY term correction, with the outcome of droplets formation.

Our motivation is concerned with the aforementioned theoretical and experimental interest, in view of existing laboratory facilities to investigate ultra-cold atomic BEC systems confined in circular and spherical geometries. By considering previous studies with single confined species, we concentrate the present analysis in clarifying the dynamical behavior of binary atomic mixture, confined within the skin of a three-dimensional (3D) spherical trap. By assuming the initial stationary condition of the binary mixture as homogeneous and trapped at the surface of a rigid sphere with radius  $R$ , the system is effectively two-dimensional (2D), with all dynamics described by the two polar angles  $\theta$  and  $\phi$ . Such simple spherical geometry with two-species confined at a surface of a bubble, hopefully, can be useful to setup initial experimental conditions for some related investigations, as well as for different other kinds of studies, such as when assuming deformed radial geometries, or by considering atomic species with more involved inter- and intra-species interactions, as the case of dipolar binary systems in spherical geometries.

For the next, this paper is structured as follows: The basic framework of the mean-field model formalism is introduced in Sec. II. In Sec. III, our approach in probing the stability of an original stationary solution is exemplified by applying the method to the non-vorticity case of a homogeneous two-species mixture. In Sec. IV, we study the stability of stationary states with quantized vortices in the shell, by considering the specific case with both species having opposite charge vorticity,  $s_2 = -s_1 = 1$ . In this case, a variational approach is shown to be helpful in establishing analytical solutions in support to the full-numerical ones. The dynamics and stability of the states are studied in detail in Sec. V, with analysis of time-evolution of the unstable modes. Finally, in Sec. VI, we present our conclusions and outlook. An appendix is also included concerning our numerical method for real-time integration of the GP equation.

## II. MODEL FORMALISM

In our present study, we assume two atomic species ( $i = 1, 2$ ) with the same mass  $M$ , which are initially within a homogeneous mixture, with both species having the same density. Apart from the theoretical convenience to consider a more symmetric initial configuration, which also will facilitate the analysis of the expected pattern results, studies with equal-mass binary systems are supported by existing BEC experiments with two-spinor states of the same isotope [16, 17]. The stability of the initial configuration will be studied by adding a small time-dependent perturbation in the initial config-

uration. For the stability, we observe that our study is concerned only with the occurrence of *dynamical instability* in the system. The possibility of *energetic instability* of the coupled condensates is not being considered in the present work, in which we have assumed zero temperature  $T$ . Energetic instabilities play role only in excited states, as they need a way to get rid of energy, which in BEC systems can be accomplished by losing the extra energy through contact with the thermal cloud [15]. They could occur in our approach only for  $T > 0$ , when having excited angular momentum states, with vortices in a spherical geometry [69, 79]. In that case, the generated vortices shall migrate to the equator-line of the sphere and being annihilated. However, for that, a dissipation mechanism is required, as interactions between the condensate with the thermal cloud. Here, we are concerned with Bose gases at effectively zero temperature; thus, in practice, there is no thermal cloud to allow a dissipation mechanism.

The inter- and intra-species interactions are given by  $g_{ij} \equiv (4\pi\hbar^2 a_{ij}/M)$ , where  $a_{ij}$  is the atom-atom scattering length. As the interaction ratio between inter-species and intra-species,  $g_{12}/g_{ii}$  (by assuming  $g_{11} = g_{22}$ ) increases, unstable modes causing inhomogeneities should appear, analogous to the one-dimensional (1D) ring case [51]. Therefore, in our following approach, we assume the two atomic species are confined in the skin of a 3D spherical shell with fixed radius  $R$ , implying on the existence of the condensate densities only inside an infinitesimal range, with  $R(1 \pm \delta/2)$ . This trapped region covering the whole sphere we can label as  $V$ , the total volume of the confinement, given by  $V \sim 4\pi R^3 \delta$ . By modeling the system with an effective  $\delta \approx 0$ , we can write the density states for each component  $i$ , with the radial function given in terms of the Dirac delta  $\delta(r - R)$ , such that  $|\Psi_i(\mathbf{r}, t)|^2 = \delta(r - R)|\psi_i(\Omega, t)/R|^2$ , where  $\Omega \equiv (\theta, \phi)$  gives the angular position in the sphere.

In order to validate approximately the assumption  $\delta \approx 0$ , we need to estimate the level energies of a trapping interaction in the radial direction, for an infinite potential well, centered in  $R$ , with radial size  $R\delta/2$  [radial wave function being zero at  $R(1 \pm \delta/2)$ ]. For a  $\delta$  enough small, the energy difference between the ground and first excited state should be enough large. For such an estimate, we can follow section VI and VII of Ref. [65], in which they consider a thicker shell for the confining region of a given condensate. By following this approach, we can verify that the single-particle radial energy excitation (ground to first excited states), in energy units  $\hbar^2/(MR^2)$ , is given by  $\mathcal{E}_R = 3\pi^2/(2\delta^2)$ . Correspondingly, in the same units, the estimated absolute value of the energy obtained from the non-linear quartic interaction term, for each species  $i$  with scattering lengths  $a_{ii}$ , with the condensed particles in the ground-state level, is given by  $\mathcal{I} = 3N_i|a_{ii}|/(4R\delta)$ . Therefore, for  $\mathcal{I} \ll \mathcal{E}_R$ , we need  $\delta \ll 2\pi^2 R/(N_i|a_{ii}|)$ . This indicates the strict range of validity of our reduction from 3D to the hard 2D sphere, which can be accomplished by controlling the two-body scattering lengths

and the number of atoms. The two-body inter- and intra-species interactions can be written as dimensionless parameters by  $\gamma_{ij} \equiv g_{ij}N_j/R^3 = 4\pi N_j(a_{ij}/R)$ , in which it was included the density dimension ( $1/R^3$ ) and the number of atoms  $N_j$ . In our case, the above estimative for the 2D reduction is given by  $\delta \ll 8\pi^3/|\gamma_{ij}|$ . In order to bring this estimate to realistic values of the physics parameters, we first note that the two-body interactions  $a_{ij}$  can be tuned by using Feshbach resonance mechanisms, with its absolute value varying from almost zero to very large values as  $100a_0$ , where  $a_0$  is the Bohr radius. On the bubble dimensions, according to Ref. [71], the radial sizes  $R$  can be of the order of 1 mm or even larger, with the bubble thickness  $R\delta$  being of the order of few  $\mu\text{m}$ . For instance, let us assume  $|a_{ij}| \sim 100a_0$ , with  $R \sim 100\mu\text{m} \approx 2 \times 10^6 a_0$ . In this case,  $|\gamma_{ij}| = 4\pi N_j|a_{ij}|/R \sim 2\pi N_j \times 10^{-4}$ , which should be within the covered range of  $|\gamma_{ij}|$  values to be considered for the strict validity of the 2D reduction that we are assuming. As realistic values for the thickness are of the order of few  $\mu\text{m}$ , we can take  $\delta \sim 10^{-2} \rightarrow 10^{-3}$ . So, a 3D treatment may be required only when very large values of  $\gamma_{ij}$  are considered. In such a case, our 2D approach is expected to provide a good approximation.

By assuming  $R$  to be our length scale, with the time unit given by  $MR^2/\hbar$ , with the states  $\psi_{i=1,2} \equiv \psi_i(\Omega, t)$  normalized to one, the original nonlinear Schrödinger equation is reduced to the following dimensionless coupled equation:

$$i\frac{\partial\psi_i}{\partial t} = \left[ \frac{1}{2}\mathbf{L}^2 + \sum_{k=1,2} (\gamma_{ik}|\psi_k|^2) \right] \psi_i, \quad (1)$$

where  $\mathbf{L} \equiv -i \left[ \hat{e}_\phi \frac{\partial}{\partial\theta} - \hat{e}_\theta \frac{1}{\sin\theta} \frac{\partial}{\partial\phi} \right]$  is the dimensionless angular momentum operator ( $\hat{e}_\phi$  and  $\hat{e}_\theta$  being, respectively, unit vectors along the azimuthal  $\phi$  and polar  $\theta$  directions), with

$$\mathbf{L}^2 \equiv - \left[ \frac{1}{\sin\theta} \frac{\partial}{\partial\theta} \left( \sin\theta \frac{\partial}{\partial\theta} \right) - \frac{1}{\sin^2\theta} L_z^2 \right], \quad (2)$$

where  $L_z^2 \equiv -\frac{\partial^2}{\partial\phi^2}$ . With the total two-component wavefunction  $\Psi(\Omega, t) \equiv \Psi[\psi_1, \psi_2]$  normalized to the number of atoms  $N$ , such that  $\int d\Omega |\Psi(\Omega, t)|^2 = N_1 + N_2 \equiv N$ , the functional energy corresponding to (1) is given by

$$E[\psi_1, \psi_2] = \sum_i \frac{N_i}{N} \int d\Omega \left[ \frac{|\mathbf{L}\psi_i|^2}{2} + \sum_j \frac{\gamma_{ij}}{2} |\psi_i|^2 |\psi_j|^2 \right]. \quad (3)$$

The inter- and intra-species two-body interactions, respectively  $\gamma_{ij}$  and  $\gamma_{ii}$ , in our approach, are assumed that in general can be repulsive ( $> 0$ ) or attractive ( $< 0$ ), with possible static and dynamical solutions being considered. Let us consider initially the non-perturbed stationary solutions of Eq. (1), normalized to one, with chemical potentials  $\mu_i$ , as given by

$$\psi_{i0} \equiv \psi_{i0}(\theta, \phi, t) = \frac{f_i(\theta)}{\sqrt{2\pi}} e^{i(s_i\phi - \mu_i t)}, \quad (4)$$

in which the  $\phi$  dependences are assumed with given charges  $s_i \in \mathbb{Z}$ , defined as the initial vorticity of the components  $i$ , which yields

$$\langle L_z \rangle_i = -i \int d\Omega \psi_i^* \frac{\partial \psi_i}{\partial \phi} = s_i \int_0^\pi d\theta \sin \theta |f_i(\theta)|^2 = s_i, \quad (5)$$

such that when non-zero can create vortices on the sphere. It is worth to stress that  $s_i \neq 0$  affects the  $f_i(\theta)$  boundary condition, due to the  $1/\sin^2 \theta$  Laplacian term, implying in  $f_i(\pi) = f_i(0) = 0$  for  $s_i \neq 0$ .

The stationary solutions of the linear part of Eq. (1) (when  $\gamma_{ik} = 0$ ) are the well-known spherical harmonics  $Y_{\ell_i, s_i}(\theta, \phi)$  ( $\ell_i = 0 \rightarrow \infty$ ,  $-\ell_i \leq s_i \leq \ell_i$ ) in which the associated Legendre functions  $P_{\ell_i, s_i}(\theta)$  are the solutions in the  $\theta$  variable. Therefore, as considering the interactions, with  $\gamma_{ik} \neq 0$ , we can generate a multiplicity of stationary solutions for a coupled system, which emerge from the linear ones. These nonlinear solutions can be continued by increasing the nonlinearity of the system.

Within our aim to follow the simplest solutions and learn about their stability, as well as the vorticity of these states when considering opposite values of the azimuthal quantum number  $s_i$  (which can be of interest in experimental setups), we start by considering the non-vorticity case, in which  $s_i = 0$ . For that, we first notice that the spherical harmonic state with  $\ell_i = 0$ , simply given by the constant  $1/\sqrt{4\pi}$ , is the ground state of the linear part and also a stationary state of the full nonlinear problem. Although, it is not necessarily the ground state of the mixture, as we should consider the miscibility of the coupled system through the intra- and inter-species interactions. In this regard, we can split the possible nonlinear stationary solutions of (3) into two distinct cases, related to the miscibility of the mixture. More precisely, by following a simple energetic consideration as given in Ref. [20], comparing the non-linear energy contribution of a complete miscible configuration, with a complete immiscible one, in which the two species are not interacting (but constrained within the same total volume), one can show that the immiscible configuration ( $g_{12} > \sqrt{g_{11}g_{22}}$ ) provides the lower energy. However, this analysis is not providing an exact relation at which the system becomes unstable. For that, a more detailed stability analysis is required, in which the trap geometry and kinetic energy term can also be relevant. This will be shown in the present case that we have the confinement region on a spherical surface.

In Sec. III we explore the stability of the uniform state to exemplify our scheme in a full analytical case without vorticity. In Sec. IV, the approach is applied to the hidden vorticity case, where we consider the  $\ell_i = 1$  solution for the linear part, with  $s_i = \pm 1$ .

The stability of these states is studied by assuming they are submitted to infinitesimal time-dependent perturbations  $u_{i\nu} \equiv u_{i\nu}(\theta, \phi)$  and  $v_{i\nu} \equiv v_{i\nu}(\theta, \phi)$ , with oscillating modes  $\omega_\nu$ , with perturbed solutions given by

$$\psi_i(\theta, \phi, t) = \psi_{i0} + [u_{i\nu} e^{-i\omega_\nu t} + v_{i\nu}^* e^{i\omega_\nu^* t}] e^{i(s_i \phi - \mu_i t)}. \quad (6)$$

By considering a linear stability analysis,  $u_{i\nu}$  and  $v_{i\nu}$  will also be associated to integer quantum numbers  $\nu$ , which are representing the perturbation modes being considered as superposition to the stationary states.

### III. HOMOGENEOUS NON-VORTICITY CASE

Let us first consider the Bogoliubov modes on top of homogeneous states with no vorticity, by following Refs. [51, 80], such that  $s_i = 0$ . By looking at the solutions of the linear part of Eq. (1), we noticed that they are given by the usual Legendre polynomials  $P_{\ell_0}(\cos \theta)$  that are eigenfunctions of  $\mathbf{L}^2$  with eigenvalues  $\ell_0(\ell_0 + 1)$ , with  $\langle L_z \rangle_i = 0$ . As instructive in the present section, for the stationary solutions we consider the simplest ground-state  $\ell_0 = 0$ , such that  $f_i(\theta) = 1/\sqrt{2}$  in Eq. (4), which also reduces the non-linear term to a constant, given by the binary interactions. Next, in order to probe the stability of these solutions under small perturbations, in our analytical approach we assume the perturbations are given by eigenfunctions of the angular momentum operator  $\mathbf{L}^2$  and  $L_z$ ; namely, the spherical harmonics,  $Y_{\ell, m} \equiv Y_{\ell, m}(\theta, \phi)$ , with  $(\ell, m)$  being the corresponding quantum numbers. Therefore, with the full angular dependence of the perturbation expanded in spherical harmonics, considering in Eq. (6)  $s_i = 0$ , with  $\nu \equiv \ell$  and the frequency oscillating modes given by  $\omega_\nu = \omega_\ell$ , we have

$$u_{i\nu}(\theta, \phi) \equiv u_{i\ell} Y_{\ell, m}, \quad v_{i\nu}(\theta, \phi) \equiv v_{i\ell} Y_{\ell, m}. \quad (7)$$

The oscillating modes are assumed in general as complex quantities,  $\omega_\ell \equiv \mathcal{R}e(\omega_\ell) + i\mathcal{I}m(\omega_\ell)$ , such that stable solutions imply  $\mathcal{I}m(\omega_\ell) = 0$  for all possible values of  $\ell$ . By replacing (6) with (7) in (1), followed by a linearization, which retains only the first order terms of  $u_{i\ell}$  and  $v_{i\ell}$  in the nonlinear part, we obtain the respective BdG coupled equations [81]. Defining  $\tilde{\ell}^2 \equiv \ell(\ell + 1)$  to simplify the following formalism, from Eqs.(1), (6) and (7), we obtain

$$\begin{aligned} \mu_i &= \sum_{k=1,2} \frac{\gamma_{ik}}{4\pi}, \\ 0 &= \left( \omega_\ell - \frac{\tilde{\ell}^2}{2} \right) u_{i\ell} e^{-i\omega_\ell t} Y_{\ell, m} - \left( \omega_\ell^* + \frac{\tilde{\ell}^2}{2} \right) v_{i\ell}^* e^{i\omega_\ell^* t} Y_{\ell, m} \\ &\quad - \sum_k \frac{\gamma_{ik}}{4\pi} \left\{ (u_{k\ell} + v_{k\ell}) e^{-i\omega_\ell t} Y_{\ell, m} + c.c. \right\}, \end{aligned} \quad (8)$$

in which the expression for  $\mu_i$  could be directly verified from Eq. (1), considering the normalization of the stationary solutions. The linear independence of  $e^{-i\omega_\ell t}$  and  $e^{i\omega_\ell^* t}$  in (8) implies in two separate equations, leading to a relation between  $u_{i\ell}$  and  $v_{i\ell}$ ,

$$\left( \omega_\ell - \frac{\tilde{\ell}^2}{2} \right) u_{i\ell} = - \left( \omega_\ell + \frac{\tilde{\ell}^2}{2} \right) v_{i\ell} = \sum_{k=1,2} \frac{\gamma_{ik}}{4\pi} (u_{k\ell} + v_{k\ell}),$$

with the solution for the oscillating modes given by

$$\omega_{\ell, \pm}^2 = \frac{\tilde{\ell}^2}{2} \left[ \frac{\tilde{\ell}^2}{2} + \frac{\gamma_{11} + \gamma_{22} \pm \sqrt{(\gamma_{11} - \gamma_{22})^2 + 4\gamma_{12}\gamma_{21}}}{4\pi} \right]. \quad (9)$$



As a general outcome from the above, we note that the solutions become unstable when assuming overall attractive interactions, such that the second term within the square brackets is negative, with absolute value larger than  $\ell(\ell+1)/2$ . In our following approach along this work, we are assuming that  $\gamma_{12} = \gamma_{21}$ , implying that the particle numbers are the same for both species ( $N_1 = N_2$ ), considering that  $g_{12} = g_{21}$  and both particles have the same mass. For the intra-species interactions, we are assuming  $\gamma_{11} = \gamma_{22}$ , which can be easily satisfied by altering the two-body scattering lengths using Feshbach resonance techniques [8]. Therefore, we obtain

$$\omega_{\ell,\pm}^2 = \frac{\ell(\ell+1)}{2} \left[ \frac{\ell(\ell+1)}{2} + \frac{\gamma_{11} \pm |\gamma_{12}|}{2\pi} \right]. \quad (10)$$

In this case, the inter-species interaction  $\gamma_{12}$  being attractive or repulsive is not relevant, as the results related to stability should be the same. The fact that the results do not depend on the sign of  $\gamma_{12}$  is related to the simple homogeneous spherical symmetry we are considering. Besides that, for  $\gamma_{11} > 0$  only the minus sign branch can be unstable subject to the condition  $|\gamma_{12}| > \gamma_{11} + \pi\ell(\ell+1)$ . Another point is that, for  $\gamma_{11} < 0$ , we can only have a small stability branch if the kinetic energy term  $\ell(\ell+1)/2$  is dominating the term inside the square brackets of (10).

Another simple possibility occurs for  $\gamma_{11} = -\gamma_{22}$  in Eq. (9), which will result that the oscillating modes become independent of the signs of both intra- and inter-species interactions ( $\gamma_{11}$  and  $\gamma_{12}$ ) given by

$$\omega_{\ell,\pm}^2 = \frac{\ell(\ell+1)}{2} \left[ \frac{\ell(\ell+1)}{2} \pm \frac{\sqrt{\gamma_{11}^2 + \gamma_{12}^2}}{2\pi} \right]. \quad (11)$$

In this case, the stability frontiers for each perturbation mode  $\ell$  are circles with radius  $\pi\ell(\ell+1)$ , due to the square brackets term.

In both cases, given by Eqs. (10) and (11), the stable and unstable regions are represented by diagrams of  $\gamma_{12}$  versus  $\gamma_{11}$  in the two panels of Fig. 1, in which the miscible phases are identified as stable regions.

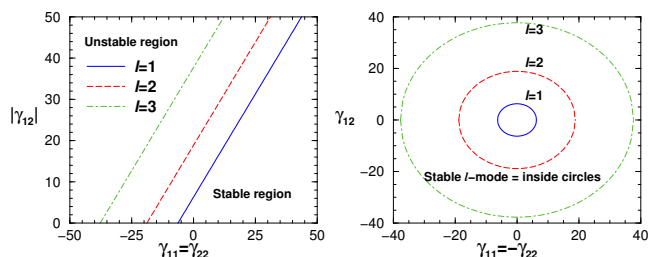


FIG. 1. (Color on-line) The stable and unstable regions are represented, for  $\gamma_{12}$  versus  $\gamma_{11}$ , indicating the miscible and immiscible phase regions respectively. In (a), for  $\gamma_{11} = \gamma_{22}$ , the stable regions are right-below the line modes with  $\ell=1, 2$ , and 3; whereas, for  $\gamma_{11} = -\gamma_{22}$  (b), they are inside circles. All quantities are dimensionless, with units defined in the text.

The present homogeneous case, with the stationary solution in the ground state, is quite simple, as verified by

the corresponding chemical potential given by Eq. (8), such that it serves the purpose to clarify the approach we are going to consider for the non-homogeneous case, with vorticity (in which we assume  $s_i \neq 0$ ). Within both conditions, (a)  $\gamma_{11} = \gamma_{22} > 0$ , given by Eq. (10), and (b)  $\gamma_{11} = -\gamma_{22}$ , given by Eq. (11), the instabilities are prescribed by the threshold for the imaginary frequency modes, which are, respectively, given by

$$\text{Im}(\omega_{\ell,-}) = \begin{cases} \pm \left[ \frac{\ell^2}{4\pi} (|\gamma_{12}| - \gamma_{11} - \pi\ell^2) \right]^{\frac{1}{2}} \Big|_{\gamma_{11}=\gamma_{22}}, \\ \pm \left[ \frac{\ell^2}{4\pi} (\sqrt{\gamma_{11}^2 + \gamma_{12}^2} - \pi\ell^2) \right]^{\frac{1}{2}} \Big|_{\gamma_{11}=-\gamma_{22}}. \end{cases} \quad (12)$$

However, we should notice that the second case ( $\gamma_{11} = -\gamma_{22}$ ) is already contained in the first case, given the following replacement:  $\gamma_{11} \rightarrow 0$  and  $\gamma_{12} \rightarrow \sqrt{\gamma_{11}^2 + \gamma_{12}^2}$ . From Eqs. (9)-(12), we can also verify that, given the nonlinear interaction term, there is a critical upper value  $\ell = \ell_{max}$ , which contributes to  $\text{Im}(\omega_{\ell,-})$ . However, it should also be clear that the lower level modes with  $\ell < \ell_{max}$  are already establishing the instability of the system.

For simplicity, in the following we select the condition  $\gamma_{11} = \gamma_{22} = 10$ , which is given by Eq. (10), for comparison of the analytical with full-numerical results. In contrast to the analytical results where we can explicitly select the angular momentum quantum numbers, in the numerical approach we start from the general perturbation form in Eq. (6) and only factor out the azimuthal exponential part of the spherical harmonics. This procedure then demands a discretization of the differential operator  $\mathbf{L}^2$  in  $\theta$  coordinate, which provides a general platform to also handle non-uniform states, as will be needed in the next section to study vortices. Consequently, within a numerical approach we have an arbitrary indexing  $\nu$  of the states according to Eq. (6), which is fixed provided that the imaginary part of the eigenvalues  $\omega_\nu$  are in decreasing order. More details of the BdG system in the numerical approach are provided in the next section.

In Fig. 2, our results are shown for the imaginary spectrum, in which the different instability modes are being explicitly identified. In panel (a), Eq. (10) is used and the modes are indexed by their angular momentum quantum number. In panel (b), the numerical results are presented using numerical diagonalization and the modes are sorted in decreasing order. The critical values for  $\gamma_{12}$  at which the instabilities start are given by  $|\gamma_{12}|_{crit} \simeq 16.28, 28.85, 47.70, \text{ and } 72.84$  for the unstable modes with  $\ell=1, 2, 3$ , and 4, respectively. Clearly, this shows that the geometry of the system can extend the stability criterium beyond the  $g_{12} > \sqrt{g_{11}g_{22}}$ , as also verified in the case of ring geometry [51].

Panels (a) and (b) of Fig. 2, with the analytical and numerical results respectively, show a notable agreement of both approaches. Nevertheless, in the numerical approach we cannot separate explicitly the total angular momentum numbers  $\ell$ , since in this case no constraints are implied a priori for  $\theta$  coordinate, providing us a general method applicable even for non-uniform stationary

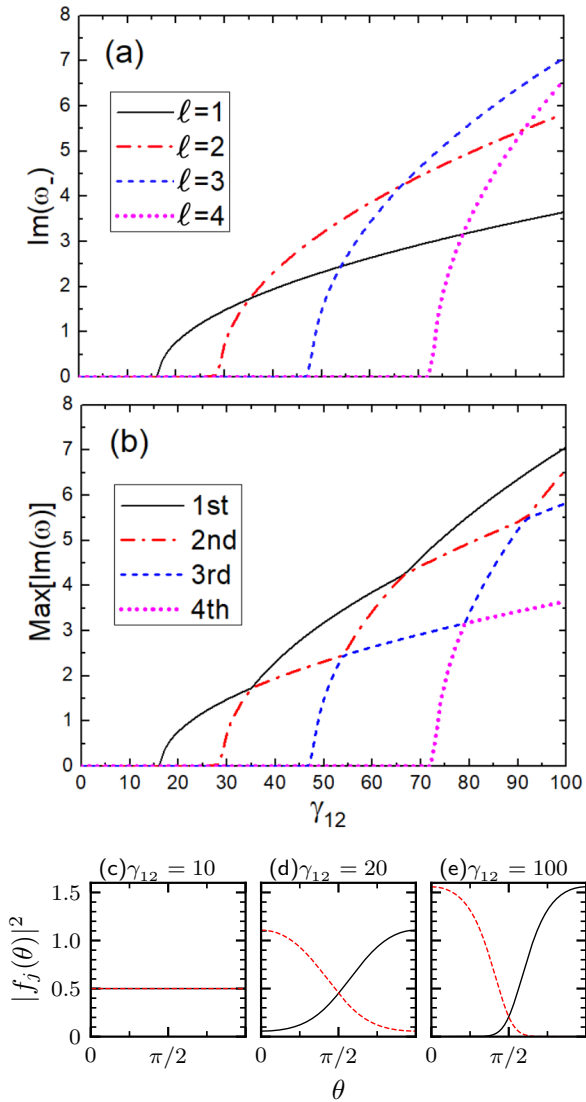


FIG. 2. (Color on-line) In frame (a), the imaginary frequency mode values [positive branch of  $\text{Im}(\omega_{\ell,-})$ , for  $\ell=1, 2, 3$ , and 4, given by Eq. (12)], are shown as functions of the inter-species interaction  $\gamma_{12}$ , by considering  $\gamma_{11} = \gamma_{22} = 10$ . In frame (b), the numerical solutions for the maximum values of  $\text{Im}(\omega_{\nu})$ , given by (6), shows the exact correspondence with frame (a), with the legend indicates the order of dominance of the modes. Correspondingly, the precise ground-state densities  $|f_j(\theta)|^2$  ( $\theta$  in rad) for both species  $j=1$  (dashed lines) and  $j=2$  (solid lines), are shown in (c), (d) and (e), for three specific values of  $\gamma_{12}$  (indicated at the top), without constraining the solutions to a uniform miscible state. Concomitantly to the appearance of the instabilities of miscible uniform state, the actual ground state enters an immiscible phase. All quantities are dimensionless, with units defined in the text.

states. Instead, we can only sort all imaginary eigenvalues in ascending order, as mentioned above. Despite this caveat, a correspondence is verified between the numerical levels of instabilities with the analytical  $\ell$ -mode solutions, such that the overall results are identical.

In Fig. 2, we also add three ground-state density plots

as function of  $\theta$  in panels (c), (d), and (e), which are obtained numerically, without constraining the species to be completely miscible. Therefore, as the instability modes grow from zero, the lowest energy state enters an immiscible phase, and the overlap becomes smaller as larger is the inter-species coupling  $\gamma_{12}$ .

The analysis of these results, obtained in a simple non-vorticity full-analytical situation, is instructive to guide us in the analysis of the instabilities that occur in vortex states.

#### IV. QUANTIZED VORTICES ON A BUBBLE

In our approach, we are assuming that both species are initially with the same density, in the lowest non-interacting stationary states  $\ell_i = 1$ , and with opposite charge vorticity between the components, given by  $s_2 = -s_1 = 1$  in Eq. (4) [15]. Therefore, we are considering initially the states within a complete miscible configuration and hidden-vorticity, whereas by hidden we mean that there is no net angular azimuthal momentum despite each species have a single charged vortex. As mentioned right after Eq. (4), this choice  $s_{1,2} = \pm 1$  implies that  $f_j(\theta)$  must vanish at the poles to avoid divergences in the kinetic energy. Therefore, homogeneous states are no longer allowed in such case of hidden vorticity (HV), which will bring more restrictions on the possibility of analytical solutions for the stationary equations and for the BdG stability analysis, when considering nonzero interaction.

From Eqs. (1), (2), and (4), we obtain the corresponding stationary eigenvalue equation, with  $f_i(\theta)$  being the eigenfunctions and  $\mu_i$  the eigenvalues, given by:

$$\begin{aligned} \mu_i f_i &= \left( \frac{1}{2} L_{s_i}^2 + \sum_{k=1,2} \frac{\gamma_{ik}}{2\pi} f_k^2 \right) f_i \\ &= -\frac{1}{2} \frac{d^2 f_i}{d\theta^2} - \frac{\cot \theta}{2} \frac{df_i}{d\theta} + \frac{s_i^2 f_i}{2 \sin^2 \theta} + \sum_{k=1,2} \frac{\gamma_{ik}}{2\pi} f_k^2 f_i, \end{aligned} \quad (13)$$

in which we are defining the dimensionless operator  $L_{s_i}^2$  as the squared angular momentum operator  $\mathbf{L}^2$  given in Eq. (2), after replacing the  $L_z^2$ -operator in favor of the corresponding azimuthal quantum number, which is  $s_i^2$  in this case. For general solutions of the above non-perturbed stationary equation, as considering different possible interactions  $\gamma_{ij}$ , which appear in the non-linear coupling term, we found appropriate to apply numerical techniques, particularly by taking into account the stability analysis which will be followed with time-dependent small perturbations. As the corresponding linear counterpart of Eq. (13) has analytical solutions which are given by the associated Legendre functions, the numerical solutions are obtained starting with an analytical continuation from non-interacting case to arbitrary interacting parameters  $\gamma_{ij}$ .

Another relevant aspect is that in our approach the initial condition is given by a complete mixed configuration

of the two species. By considering that, in the following, we introduce a variational solution analysis for HV states, which will be compared with the corresponding full-numerical results.

### A. Variational treatment - homogeneous case

For a variational solution, we consider here the vorticity case with  $s_1 = -s_2 = 1$ , for which the lowest level provided by the linear solution is given by  $\ell = 1$ . Therefore, for such homogeneous case, we assume the corresponding linear solutions  $f_i = \sqrt{3/4} \sin \theta$  being identical for both species and modified by a variational parameter  $\beta$ , such that  $f_v^2 = \lambda(\sin \theta)^\beta$ , with  $\lambda$  given by the normalization of  $f_v$ . This variational solution is obviously limited to  $\beta > 0$ , in order to have a normalized wave function. With the above assumptions, the non-linear inter- and intra-species interaction parameters can be replaced by a single parameter  $\gamma \equiv \gamma_{11} + \gamma_{12}$ . The component wave functions are given by  $\psi_v \equiv \psi_1 = \psi_2 = \sqrt{1/(2\pi)} f_v(\theta)$ , where  $f_v \equiv f_v(\theta) = \sqrt{\lambda(\sin \theta)^\beta}$ , are normalized such that

$$\int d\Omega |\psi_v|^2 = \lambda \int_0^\pi d\theta (\sin \theta)^{\beta+1} = \lambda \mathcal{J}(\beta) = 1, \quad (14)$$

from where we have an integral definition for  $\mathcal{J}(\beta)$ , with the following properties ( $\beta > 0$ ):

$$\begin{aligned} \mathcal{J}(\beta) &= \frac{\beta}{\beta+1} \mathcal{J}(\beta-2), \\ \frac{d\mathcal{J}(\beta)}{d\beta} &= \int_0^\pi d\theta (\sin \theta)^{\beta+1} \ln(\sin \theta). \end{aligned} \quad (15)$$

With the above, the total energy (3) can be written as a function of  $\gamma$  and  $\beta$ ,

$$\begin{aligned} E(\gamma, \beta) &= \frac{(\beta+2)^2}{8\beta} + \frac{\gamma}{4\pi} \frac{\mathcal{J}(2\beta)}{[\mathcal{J}(\beta)]^2} \\ &= \frac{(\beta+2)^2}{8\beta} + \frac{\gamma}{8\pi} \frac{(\beta+1)^2}{\Gamma(2\beta+2)} \left[ \frac{\Gamma(\beta+1)}{\Gamma(\frac{\beta}{2}+1)} \right]^4 \end{aligned} \quad (16)$$

where the nonlinear term was expressed in terms of the well-known gamma functions,  $\Gamma(\zeta)$  [which is an extension of integer number factorial  $\Gamma(n) = (n-1)!$ ]. Therefore, by minimizing  $E(\gamma, \beta)$  for the parameter  $\beta$ , we obtain a relation between  $\gamma$  and the variational  $\beta$ , such that we have also the corresponding minimized energies, given as  $E_{var}(\beta)$ . The results of this variational procedure are displayed in the Fig. 3. In the left panel (a) we show the functional relation between the variational parameter  $\beta$  and the interaction parameter  $\gamma = \gamma_{11} + \gamma_{12}$ ; and, in the right panel (b) we present the variational results for the energy and chemical potential as functions of  $\gamma$ , together with the exact numerical results. As verified the variational results are providing the *almost exact* solutions, even for very large non-linearities. The chemical potential, also shown, can be obtained directly from  $E_{var}(\beta)$ ,

$$\mu_{var}(\beta) = 2E_{var}(\beta) - \frac{(\beta+2)^2}{8\beta}. \quad (17)$$

In case of attractive overall interactions ( $\gamma_{11} + \gamma_{12} < 0$ ) we observe in the left panel of Fig. 3 that the minimization of the energy will correspond to increasing values of  $\beta$ . In order to clarify the limit for large negative  $\gamma$ , we can apply in Eq. (16) the well-known Stirling's formula, derived for real positive variables  $z \gg 1$  (shown to be valid even for relatively low values of  $z$  [82]), given by  $\Gamma(z+1) \sim \sqrt{2\pi z} (z/e)^z$ . With this expression, for  $\beta \gg 1$ ,

$$\begin{aligned} \frac{(\beta+1)^2}{\Gamma(2\beta+2)} \left[ \frac{\Gamma(\beta+1)}{\Gamma(\beta/2+1)} \right]^4 &= e \sqrt{\frac{1}{2\pi}} \frac{(2\beta+2)^2 (2\beta)^{(2\beta)}}{(2\beta+1)^{(2\beta+3/2)}} \\ &\sim e \sqrt{\frac{\beta}{\pi}} \left( \frac{2\beta}{2\beta+1} \right)^{2\beta} = \sqrt{\frac{\beta}{\pi}}. \end{aligned} \quad (18)$$

By replacing (18) in (16), in the asymptotic region, the variational energy obtained for  $\gamma < 0$  is given by

$$E(\gamma, \beta) \sim \frac{\beta}{8} - \frac{|\gamma|}{8\pi} \sqrt{\frac{\beta}{\pi}}. \quad (19)$$

The minimization of the energy will give us  $\beta_{min} = |\gamma|^2/(4\pi^3)$ , with the corresponding negative energy going asymptotically as  $-\beta_{min}/8$ . By removing the  $\beta$ -dependence, for asymptotically large negative interactions, we obtain the energy and chemical potential as

$$E(\gamma) \sim -\frac{|\gamma|^2}{32\pi^3}, \quad \mu \sim -\frac{3|\gamma|^2}{32\pi^3}. \quad (20)$$

We should also observe that the corresponding variational densities, given by  $|f_v(\theta)|^2 = (\sin \theta)^\beta/[2\pi\mathcal{J}(\beta)]$ , goes to a Dirac-delta function representation located at  $\pi/2$ , when  $\beta \rightarrow \infty$ . This is being represented in panel (a) of Fig. 4, for a few values of the interaction parameter  $\gamma \equiv \gamma_{11} + \gamma_{12}$ , in which variational results identified by the corresponding values of  $\beta$  are being compared with exact-numerical ones. The results for the densities are quite representative of the deviations between exact and variational results (deviations which are partially hidden in the observables as energy and chemical potentials). Therefore, to enhance the deviation between variational and exact results, the density peaks are shown in panel (b) as a function of  $\gamma$ .

### B. Bogoliubov-de Gennes stability analysis

Once verified the non-perturbed stationary solutions, their stability is probed by considering the time-dependent analysis, considering small perturbations. Due to the strict phase dependence of  $\phi$  for the stationary state  $\psi_{i0}$  in Eq. (4), it is convenient to follow by expanding the perturbed states in an angular momentum basis, as done in Ref. [81]. By separating the azimuthal dependence  $\phi$  as a phase with quantum number  $m$ , let us consider in Eq. (6), the infinitesimal time-dependent perturbations with the coefficients  $u_{i\nu}$ ,  $v_{i\nu}$  replaced by

$$u_{im}(\theta, \phi) \equiv u_{im}(\theta) e^{im\phi}, \quad v_{im}^*(\theta, \phi) \equiv v_{im}^*(\theta) e^{-im\phi}. \quad (21)$$

By factoring the azimuthal dependence, in the next, we follow by defining  $u_{im} \equiv u_{im}(\theta)$  and  $v_{im} \equiv v_{im}(\theta)$ . The corresponding BdG equations, which can be solved numerically for given integers  $m \in \mathbb{Z}$ , can be derived by

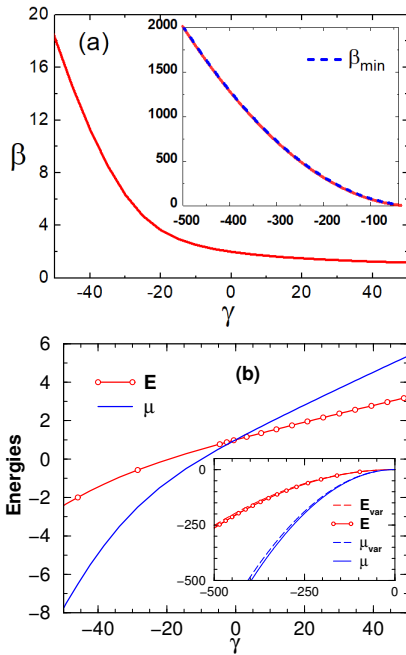


FIG. 3. (Color on-line) In terms of the summed interaction parameters  $\gamma \equiv \gamma_{11} + \gamma_{12}$  (with  $\gamma_{11} = \gamma_{22}$ ), in panel (a) we have the minimization variational parameter  $\beta$ . In panel (b), an almost perfect agreement between variational and exact-numerical results are shown for the energies and chemical potentials. In both panels (a) and (b), the corresponding attractive asymptotic results are shown in the insets. All quantities are dimensionless, with units defined in the text.

substituting the coefficients defined by Eq.(21) in the corresponding differential nonlinear equation [81].

From that, by considering the chemical potentials  $\mu_i$ , with the corresponding eigenfunctions  $f_i(\theta)$ , as given in Eq. (13), the corresponding set of coupled equations for  $(u_1, v_1, u_2, v_2)$ , is given by the following BdG matrix:

$$\begin{pmatrix} \mathcal{D}_1^+ & \alpha_{11} & \alpha_{12} & \alpha_{12} \\ -\alpha_{11} & -\mathcal{D}_1^- & -\alpha_{12} & -\alpha_{12} \\ \alpha_{21} & \alpha_{21} & \mathcal{D}_2^+ & \alpha_{22} \\ -\alpha_{21} & -\alpha_{21} & -\alpha_{22} & -\mathcal{D}_2^- \end{pmatrix} \begin{pmatrix} u_1 \\ v_1 \\ u_2 \\ v_2 \end{pmatrix} = \omega \begin{pmatrix} u_1 \\ v_1 \\ u_2 \\ v_2 \end{pmatrix}. \quad (22)$$

In the above, we are defining  $\alpha_{ij} \equiv \gamma_{ij} f_i f_j / (2\pi)$  and  $\mathcal{D}_i^\pm \equiv (L_{s_i \pm m}^2) / 2 - \mu_i + (2\gamma_{ii} f_i^2 + \gamma_{ij} f_j^2) / (2\pi)$  ( $i \neq j$ ). By given the values of  $m$  and  $s_i$ , this system can be solved numerically. Also, by considering Eq. (2), if one looks for a simplification of the matrix elements, we can identify the following relations between the operators  $\mathcal{D}_i^\pm$ : One, which is in general given by  $\mathcal{D}_1^+ - \mathcal{D}_1^- = \mathcal{D}_2^- - \mathcal{D}_2^+ = 2m / \sin^2 \theta$ ; and another, valid for  $\gamma_{11} = \gamma_{22}$ ,  $\gamma_{12} = \gamma_{21}$ :  $\mathcal{D}_1^+ - \mathcal{D}_2^- = \mathcal{D}_1^- - \mathcal{D}_2^+ = \mu_2 - \mu_1 = 0$ . With these relations, the four operators appearing in the diagonal part of (22) can be reduced to just one operator, such that  $\mathcal{D}_1^- + \omega = \mathcal{D}_1^+ + \omega - 2m / \sin^2 \theta$ ,  $\mathcal{D}_2^+ - \omega = \mathcal{D}_1^+ - \omega - 2m / \sin^2 \theta$ ,  $\mathcal{D}_2^- + \omega = \mathcal{D}_1^+ + \omega$ .

Despite the general analytical treatment presented so far for the BdG equations, we restrict the analysis to the stability of a mixture that was initially in a fully miscible configuration, with  $\gamma_{11} = \gamma_{22}$  and  $f_1(\theta) = f_2(\theta) \equiv f(\theta)$ . Within the present assumptions, with  $s_1 = -s_2 = 1$ , the

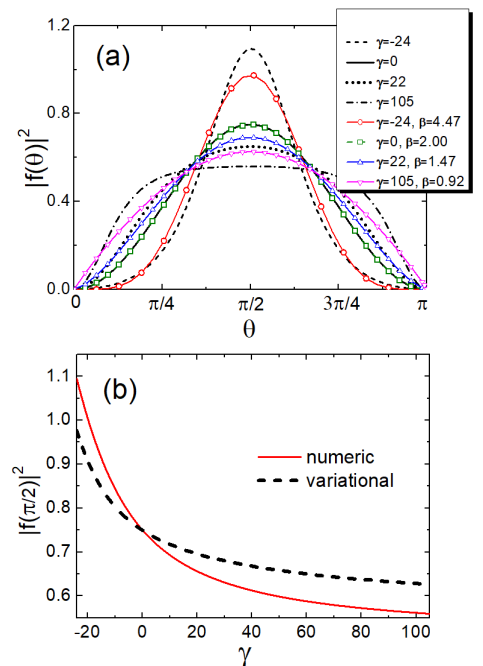


FIG. 4. (Color on-line) In the panel (a), considering four values of  $\gamma$ ,  $|f(\theta)|^2$  variational results (with  $\beta$  indicated) are being compared with the full numerical ones. In the panel (b), the density peaks  $[1/\mathcal{J}(\beta)]$ , for the variational case] are shown as functions of  $\gamma \equiv \gamma_{11} + \gamma_{12}$  ( $\gamma_{11} = \gamma_{22}$ ). All quantities are dimensionless, with units defined in the text.

numerical approach requires first to solve Eq. (13), and then use the resulting  $f(\theta)$  in Eq. (22). In Sec. III we have a particular case with  $s_j = 0$  and  $f_i(\theta)$  constant, with the given numerical results for  $\gamma_{11} = 10$  shown in panel (b) of Fig. 2.

The numerical solution of Eq. (13) is determined by using the Newton Conjugate-Gradient (NCG) method, which is suitable for analytical continuation from a known solution for a particular case [83]. The starting point is taken from the noninteracting case, which has the associated Legendre functions as general solutions,  $P_\ell^s(\cos \theta)$ , with  $s = \pm 1$  and  $\ell = 1$ , corresponding to the lowest energy level providing the HV condition, which also implies that  $\mu = 1$ . Nevertheless, it is worth emphasizing that we have a full spectrum also when considering higher angular momentum  $\ell$  that can be obtained using this analytic continuation procedure.

## V. STABILITY AND DYNAMICS OF HIDDEN VORTICITY STATES

In this section, we investigate the stability of the coupled stationary states (with their corresponding vorticity established by  $s_1 = -s_2 = 1$ ) under small time-dependent oscillatory perturbation as given by (21). The instabilities are being verified for different modes of perturbations, which are numerically identified by the quan-



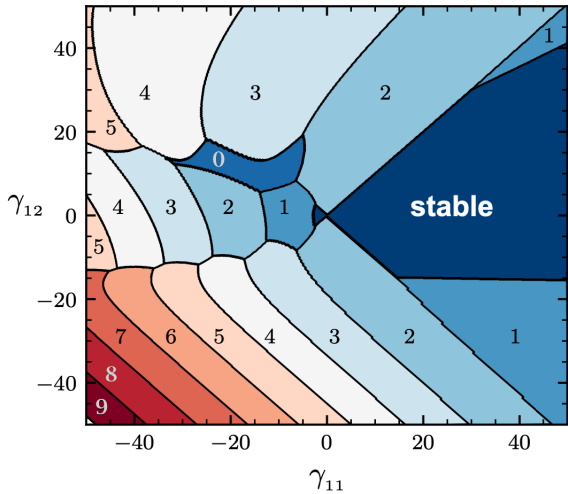


FIG. 5. (Color on-line) Stability diagram, in a phase space defined by the inter-species  $\gamma_{12}$  versus the intra-species interactions  $\gamma_{11} = \gamma_{22}$ , for  $|\gamma_{ij}| < 50$ . The dark area is the stable region, with the unstable ones dominated by perturbation modes with  $m$  up to 9 (as indicated). In all the cases, the vorticity is given by  $s_1 = -s_2 = 1$ . The  $\gamma_{ij}$  interactions are dimensionless, with units defined in the text.

tum number  $m$  appearing in (21). Therefore, systematically, by solving the corresponding GP formalism, we obtain the lowest order unstable modes. As considering the symmetry of the solutions, which are identical for positive and negative values of  $m$ , in our following analysis we are just referring to the positive values, with  $m$  starting from 0.

Concerning our general study for the stability of the system, we are summarizing the results in the diagram shown in Fig. 5, in which the phase space is defined by the inter- and intra-species interactions, with  $\gamma_{11} = \gamma_{22}$ . In this diagram, for the intra- and inter-species interactions, we are assuming both possibilities that they can be repulsive  $\gamma_{ij} > 0$  or attractive  $\gamma_{ij} < 0$ , varying from  $-50$  up to  $50$ , with the only restriction that the intra-species interactions are identical for both species. The diagram is indicating the stable and unstable regions with the corresponding predominant modes, which is the one with the largest imaginary part, following the same procedure as we have considered for the homogeneous case shown in Fig. 1. However, by considering the inhomogeneous case, it is worth to emphasize the very different behaviors depending on whether some of the interaction parameters can be negative. In this case, the diagram is indicating the instability region, considering the dominant unstable mode, from  $m = 0$  up to  $m = 9$ . This highlights important features, since we can see how many modes simultaneously can destabilize the system, as well as their magnitude, which is important by analyzing the full numerical solution of the time-dependent problem.

In general, as verified in Fig. 5, many modes start to compete as  $|\gamma_{12}|$  increases, even more rapidly for the attractive region. Moreover, it is also important to note

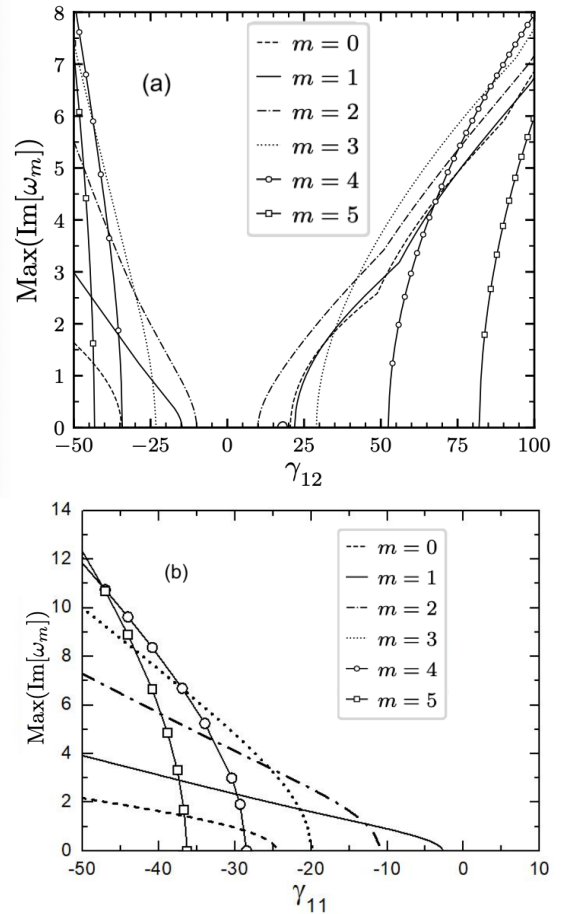


FIG. 6. The above two panels, (a) and (b), refer to the imaginary spectrum of the BdG equations, given by the  $\text{Im}(\omega_m)$ , with unstable modes up to  $m = 5$ . They correspond to two lines of Fig. 5. The panel (a) is obtained by varying  $\gamma_{12}$  with fixed  $\gamma_{11} = 10$ ; with the panel (b), by varying  $\gamma_{11}$  with fixed  $\gamma_{12} = 0$ . As in Fig. 5, the vorticity is for  $s_1 = -s_2 = 1$ . All quantities are dimensionless, with units defined in the text.

from this diagram that the binary system can be stable mainly for  $\gamma_{11} > 0$ , with repulsive and attractive inter-species  $\gamma_{12}$  within some ranges. Besides that, we can also observe a small stable interval for  $\gamma_{11} < 0$ , when the inter-species absolute value  $|\gamma_{12}|$  is comparable with  $\gamma_{11}$ , which is related to the necessary energy at which we have the kinetic energy dominating, together with the interplay between attractive and repulsive non-linear interactions. As in the other regions, which are stable under small time-dependent perturbations, we have confirmed the stability of this particular region. For example, by considering  $\gamma_{11} = -2.0$  with  $\gamma_{12} = 0$ , the corresponding state remains stable for a larger time interval, going till  $t = 100$ , which we found enough for any manifestation of instability.

In Fig. 6 our results are concentrated in two specific cases, in order to help elucidating the results shown in the diagram, and expose the relevance of the different

modes to generate the instabilities. In these two plots, we are considering the particular behavior of the maximum values of the unstable modes, for fixed values of one of the interactions. In the panel (a) we fix the intra-species interactions, with  $\gamma_{11} = 10$ , with the inter-species interaction  $\gamma_{12}$  varying in a larger interval than the one shown in Fig. 5, from  $-50$  up to  $+100$ . The stable regions are clearly identified as the ones for  $|\gamma_{12}| \leq \gamma_{11} = 10$ , in this case, with the first dominant unstable mode being for  $m = 2$ . The competing behaviors of all the unstable modes, up to  $m = 5$ , are shown in this panel, at which the dominant modes (for the instability) are the ones with the largest values for the  $Im(\omega_m)$ . In panel (b) of Fig. 6, we present the corresponding spectrum for the case  $\gamma_{12} = 0$ , in which the system is uncoupled, such that both species 1 and 2 have the same spectrum, considering that we are assuming  $\gamma_{11} = \gamma_{22}$ . This figure, more than indicating the stable regions shown in Fig. 5, also clarifies how the different modes contribute to the instability.

From the initial form of the perturbations, given by Eqs. (6) and (7), we interpret imaginary values of  $\omega$  as an exponentially growing perturbation, which in turn shows that, after some evolution period, the perturbations should not be assumed small in comparison with the condensate wave functions (4), as initially assumed to obtain the BdG equations. This implies that any initial perturbation different from zero will drastically change the condensate state after a sufficiently long time. To analyze such effect, we just use the respective stationary state obtained numerically as the initial condition in the full time-dependent problem represented of Eq. (1), whereas any exponentially raising perturbation is triggered by the numerical noise.

As a main measure to track both species density behavior, we introduce a functional for the miscibility of both time-dependent densities  $|\psi_i|^2 \equiv |\psi_i(\theta, \phi, t)|^2$ , defined by

$$\Lambda[\psi_1, \psi_2] \equiv \frac{[\int d\Omega |\psi_1|^2 |\psi_2|^2]^2}{\int d\Omega |\psi_1|^4 \int d\Omega |\psi_2|^4}, \quad (23)$$

which is one for complete overlap of the densities (miscible mixture); reducing to zero when the coupled system is completely immiscible. In the following we present our main results, exemplified by the case with intra-species interactions fixed at  $\gamma_{11} = \gamma_{22} = 10$ . For the inter-species interaction, we present results for repulsive and attractive cases. The general diagrams presented in Fig. 5 indicate that similar features could be verified for other values of the interactions.

In the next section, our main results are illustrated with the analysis of the dynamics of few representative cases considering repulsive and attractive inter-species cases. We are mainly focused on the cases that we have repulsive intra-species interactions.

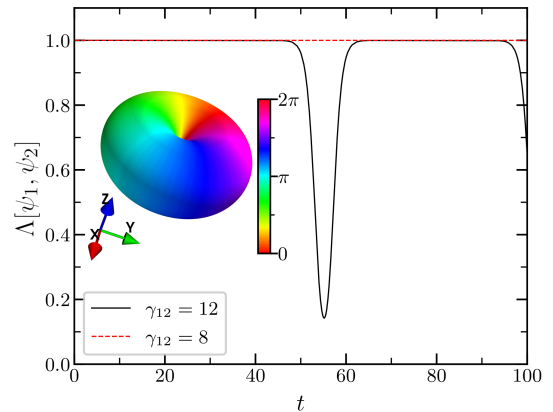


FIG. 7. (Color on-line) Time evolution of the two-species overlap for a hidden vorticity mixture state with  $s_1 = -s_2 = 1$  and  $\gamma_{ii} = 10$ , in a stable ( $\gamma_{12} = 8$ , with dashed line) and an unstable ( $\gamma_{12} = 12$ , with solid line) region. At  $t \approx 48$ , with  $\gamma_{12} = 12$ , the miscibility suffers a short pulsed change from the initial condition, which is verified to be periodic in a longer-time interval (See Fig. 8). The radial density 3D representation is for the initial condition of  $|f_1(\theta)|^2$  with  $\gamma_{12} = 12$ , in which the phases around the surface are mapped to colors (The corresponding 1D plot of  $|f_1(\theta)|^2$  is in Fig. 4, with  $\gamma_{11} + \gamma_{12} = 22$ ). All quantities are dimensionless, with units defined in the text.

#### A. Dynamics of unstable states - repulsive inter-species case

The result for time evolution of the miscibility functional (23) is presented in Fig. 7, considering a time interval  $t < 100$ , in which we are comparing the time evolution of two states subject to different stability conditions. As verified, when using  $\gamma_{12} = 8$  the overlap between the two states remains complete. However, it appears an unstable branch for  $\gamma_{12} > 10$ . As can be noted, in agreement with the BdG prediction, for  $\gamma_{12} = 12$  case the overlap changes drastically near  $t \approx 48$ , indicating that indeed some perturbation became relevant to the condensate wave function, growing from initial numerical finite precision. Meanwhile, there is no change in the density profile for both species for  $\gamma_{12} = 8$  as expected since it is stable against small perturbations. Near the final time observed,  $t \approx 90$  the overlap starts to change again after a period remaining in the initial value. A sketch of the initial state is also provided as a surface plot where the radius of the surface was taken as  $|f_1(\theta)|^2$ , that is equal to  $|f_2(\theta)|^2$ , but their phases have different orientations as  $s_1 = -s_2 = 1$ , which are displayed in colors over the surface. For a more complete picture, we have verified the time evolution of the miscibility for a longer time interval, shown in Fig. 8.

Analyzing Fig. 7 carefully, for this initial condition we see that after a brief period, the overlap functional  $\Lambda$  becomes smaller than 1, approximately for  $t \in [45, 65]$ , it stands for a long period in its initial value, up to  $t \approx 92$ , when it starts to decrease again. Therefore, naturally

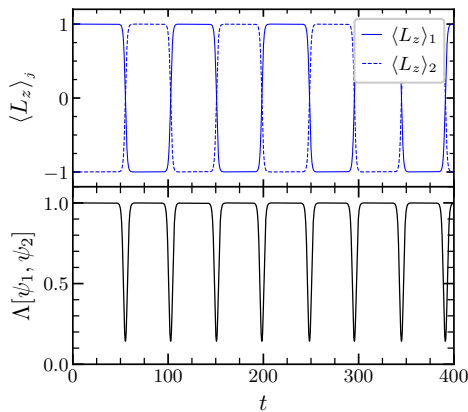


FIG. 8. For the same conditions given in Fig. 7, we show the corresponding long-time evolution (up to  $t = 400$ ) of the two-component angular momenta,  $\langle L_z \rangle_i$  (upper panel), with the associated density overlap  $\Lambda$  (lower panel). A clear periodic behavior is verified for both. All quantities are dimensionless, with units defined in the text.

arises the question of whether this behavior is periodic or not. In Fig. 8, we can confirm the periodic behavior not only for  $\Lambda$ , but also for the angular momentum of both species in a long time dynamics. Nevertheless, the period of the angular momentum of each species is twice the period of  $\Lambda$  and it reveals an interesting feature as the species exchange their momenta between  $\pm 1$  as  $\Lambda$  returns to 1.

The oscillating period inferred from Fig. 8 was  $\tau = 47 \pm 1$  for  $\Lambda$ . To obtain the period, we used the  $\Lambda < 0.2$  points as suggested by the minimum in Fig. 7, and computed time instants where the derivative vanished, from which we computed the average and standard deviation (explaining the  $\pm 1$  in  $\tau$ ). However, it is worth emphasizing that this value depends on how the instability is triggered. In our case, it is due to the finite precision of numerical calculations.

In Fig. 9 we provide some snapshots of the density at  $t = 55$  of both species illustrated by colors in a spherical shell. As can be seen, not only the BdG prediction can be confirmed as the instability mode grew and changed completely the initial density profiles, that were independent of  $\phi$  angle, but also the density for both species breaks up in 2 disconnected pieces along the  $\phi$  angle in the spherical shell, which corroborates with a superposition of modes with spatial frequency  $m = \pm 2$ . Specifically in this case, corresponding to  $\gamma_{12} = 12$  in Fig. 6(a), only  $m = 2$  contributes, explaining why we should expect only two pieces in the dynamical breakup, although it is not a rule when more than one mode is unstable.

Finally, we explore another case with large inter-species interaction in real-time evolution, using  $\gamma_{12} = 95$  still for  $\gamma_{11} = \gamma_{22} = 10$  in Fig. 10. The two first columns refer to the first species densities, while the last two correspond to the second, in different view angles as denoted

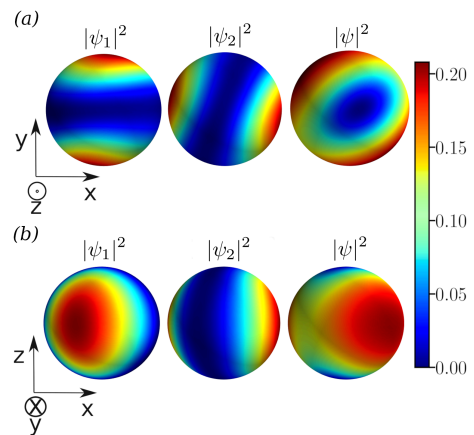


FIG. 9. (Color on-line) Density plots for both species and average density at  $t = 55$  of the dynamics presented for  $\gamma_{12} = 12$ . Frame (a) displays the images with  $z$  axis pointing outwards the page while frame (b) provide a  $90^\circ$  rotation with respect to (a), with  $y$  axis pointing inwards the page. All quantities are dimensionless, with units defined in the text.

by the axes legend at the bottom. At the initial instant, both species share the same density profile, which can also be seen as a 1D plot in Fig. 4, vanishing at the top due to HV condition. In a second instant  $t = 3.85$  in the row (b) we already can see the formation of 4 localized peaks around the sphere along  $\phi$  direction, though the contrast is not so prominent. In a third instant  $t = 4.15$  let clear the immiscibility of the mixture with 4 localized and narrow peaks. The color scale showed for each instant provide a quantitative comparison for the density clustering of the 4 pieces.

There is a sharp contrast between the two cases evaluated in Fig. 9 and Fig. 10 in the time elapsed until the unstable mode becomes dominant, in the first case at  $t \approx 48$  and in the second  $t \approx 3.8$ . This is explained by the magnitudes of the imaginary part of the BdG eigenvalues provided in Fig. 6, and more rapidly the mode will destabilize as larger is  $\gamma_{12}$ , though we cannot expect any proportional relation as the initial numerical inaccuracy that triggers these modes is hard to estimate. However, Fig. 6 points out that the region  $\gamma_{12} = 95$  has many competing modes while in  $\gamma_{12} = 12$  there is only the  $m = 2$  mode as unstable, and in contrast to the periodic behavior observed in the latter case, in Fig. 11 we can see that no clear pattern can be detected. We attribute the unrecognizable pattern in the time evolution as a consequence of many modes excitation.

## B. Dynamics of unstable states - attractive inter-species case

The case of attractive inter-species interaction was also explored in our study, as shown in the diagram given in Fig. 5 and by the stability spectrum shown in Fig. 6.

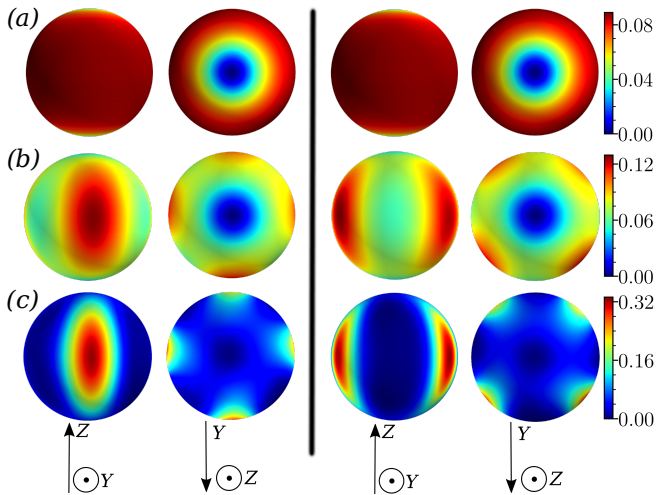


FIG. 10. (Color on-line) Density time-evolution for the coupled system with  $m = 4$  dominant unstable mode. The first two columns are for the species 1, with the remaining two columns for the species 2, considering two visualization angles, as indicated in the graphical legends at the bottom. The upper row (a) represents the two densities at the initial stage  $t = 0$  (when both species are completely mixed,  $|\psi_1|^2 = |\psi_2|^2$ ). The middle row (b) is for an intermediate time  $t = 3.85$ , with the system partially immiscible with four maxima being distinguished already in the sphere. In the lower row (c),  $t = 4.15$ , we have already a final complete immiscible configuration with the density peaks well localized on the sphere, at different positions. The interaction parameters are  $\gamma_{11} = \gamma_{22} = 10$  and  $\gamma_{12} = 95$ , with the initial condition obtained by the lowest energy state with  $s_1 = -s_2 = 1$ . The time instants are dimensionless, with units given in the text.

In contrast to the repulsive cases, when the two species are prone to breaking down into immiscible pieces, the attractive interaction should maintain the overlapping densities as initially prepared in the stationary state, as being energetically favorable. Therefore, they shall maintain the miscibility, with the unstable modes indicating that it will not be uniform in the azimuthal  $\phi$  direction.

In Fig. 12 we provide an example of real-time evolution of unstable HV state with  $\gamma_{12} = -34$  and  $\gamma_{11} = \gamma_{22} = 10$ . During all the time observed, both species have complete overlap, with  $\Lambda = 1$ . The instability starts growing drastically for  $t \gtrsim 7$ , being dominated by the  $m = 3$  mode, which can also be followed by looking at our diagrammatic representation given in Fig. 5, corresponding to the largest imaginary part in the BdG spectrum. More closely, the dominance of the mode  $m = 3$  for  $\gamma_{12} = -34$  is also shown in Fig. 6. The dominance of this mode implies in the densities being broken into three pieces around the sphere. From the time instant  $t = 7$ , when the densities start to be accumulated at different positions on the sphere, we show snapshots of them at  $t = 7.6$  and  $t = 8.0$ . In the upper row, with  $|\psi_1|^2 = |\psi_2|^2$ , both densities are shown by color-density plots. In the lower row, the full wave function is represented by using a ra-

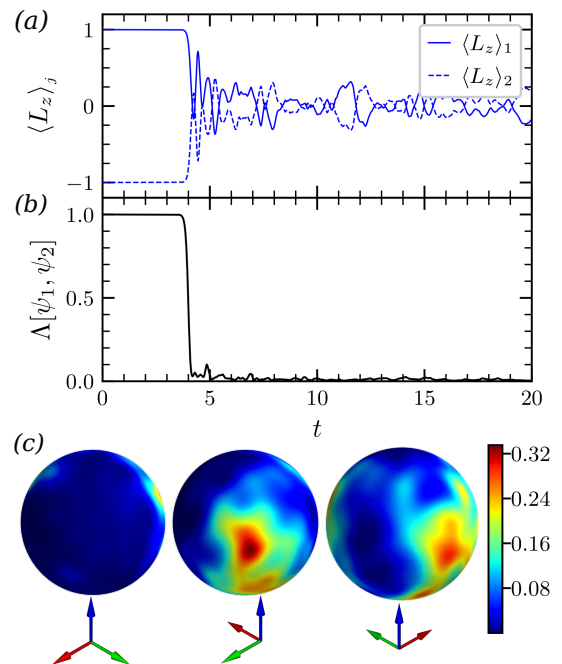


FIG. 11. (Color on-line) The time evolution for  $0 < t < 20$  is shown for  $\langle L_z \rangle_i$  (a) and for the overlap  $\Lambda$  of the two components (b), considering the unstable hidden vorticity state  $s_1 = -s_2 = 1$  with  $\gamma_{ii} = 10$  and  $\gamma_{12} = 95$ . A drastic variation is verified close to  $t = 4$ . In (c), three different angle views of the density distribution are selected for the species 1 at  $t = 16$ . All quantities are dimensionless, with units defined in the text.

dial surface plot for the densities, with a color mapping for the phase, with the  $z$ -axis tilted. The numerical solution could be evaluated up to  $t = 8.1$ , as at this instant the condensate wave functions start to become singular in the numerical grid, breaking the energy and norm conservation. Despite both methods of visualization are complementary, especially at  $t = 8.0$  when the condensates are about to collapse, the radial plot is more suitable to see the three peaks. The two-species angular momentum values,  $\langle L_z \rangle_i$ , are also provided for completeness, with both being zero at the collapse instant.

In this case shown in Fig. 12, the attractive inter-species interaction  $\gamma_{12} = -34$  is dominating against the repulsive intra-species one, given by  $\gamma_{11} = 10$ . Therefore, effectively, we have an overall attractive interaction with the system collapsing. Indeed, in the beginning we observe the instability of the mode  $m = 3$  which split the condensate into three pieces. Next, after a short time interval, the effective attraction shrinks the localized densities till the collapse.

## VI. CONCLUSIONS AND PERSPECTIVES

Summarizing our main outcome, we provide a dynamical stability study of a binary Bose-Einstein condensed



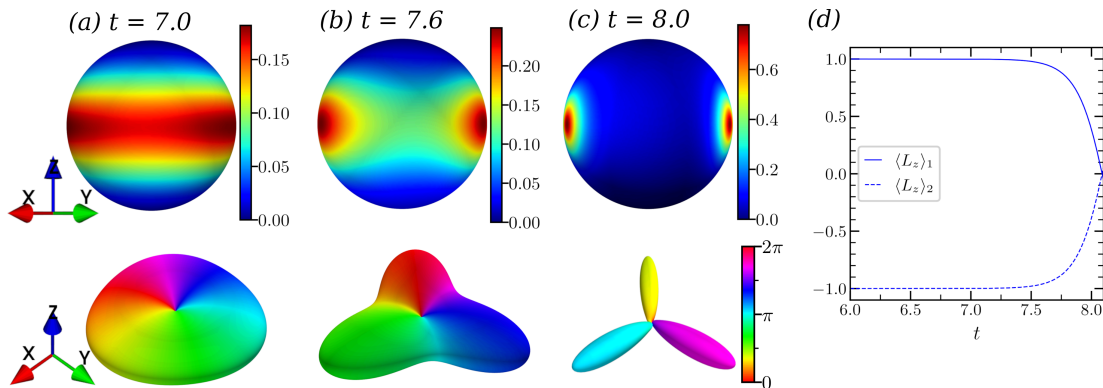


FIG. 12. (Color on-line) Density plots  $|\psi_1|^2 = |\psi_2|^2$ , in the inter-species attractive case with  $\gamma_{12} = -34$  and  $\gamma_{ii} = 10$ , within a completely miscible configuration ( $\Lambda = 1$ ). Three-time instants close to the collapse are shown, for  $t=7.0$  (a), 7.6 (b), and 8.0 (c), with the instability dominated by  $m = 3$ . In the upper row, they are mapped to colors on the sphere surface (central visualization at  $\theta = \pm\pi/2$ ). The maxima are in three  $\phi$  positions, which are best verified in the lower row with  $z$ -axis tilted by  $45^\circ$ , where the densities have radial representation with the phases mapped to colors. In panel (d), we have the two-species time evolution  $\langle L_z \rangle_i$ , close to the collapse. The initial condition is for the lowest energy state with  $s_1 = -s_2 = 1$ . All quantities are dimensionless, with units given in the text. In the Supplemental Material [84], a movie illustrates the corresponding full-time evolution of the density till the collapse.

mixture trapped on the surface of a rigid spherical shell, exploring the miscibility of the system with and without vortex charges. For that, the initial stationary solutions are treated by using the usual GP mean-field approach, within two possible configurations. First, with both species within a homogeneous non-vorticity mixture; next, when the initial configuration is in the lowest non-interacting stationary states, with opposite charge vorticity. The stationary solution study is supplemented by a variational analysis for the specific case in which the non-linear system is with both species at the lowest level ( $\ell = 1$ ) that allows the existence of hidden vorticity.

In our approach to explore the stability of the system, we consider the Bogoliubov-de Gennes method, in which the stationary non-linear formalism is submitted to a linearization, with small time-dependent perturbation modes. The analysis of both the cases, with and without vortex charges, is followed by computing the critical points at which the system becomes unstable.

The relevance of the different modes to generate the instabilities is being exposed in the sample results presented in the panels of Fig. 6, which are obtained numerically for a large range of repulsive and attractive interactions. From this kind of analysis, a complete diagram is provided in Fig. 5, in the phase space defined by the inter- and intra-species interactions, where we can verify the stable regions, together with the dominating unstable modes. In all these cases, we assume opposite charge vorticity in the lowest initial stationary states.

The study of the dynamics of the mixture is being represented by the time evolution of the miscibility, given by the overlap of the densities, together with the angular momentum distribution of the two species. For this purpose, we select a few cases to characterize stable and different unstable regimes. In the selected examples, where

we kept fixed and repulsive the intra-species interactions, we illustrate the time-evolution of the coupled densities distributed in the bubble surface, by considering immiscible and miscible regimes, which are, respectively, given by repulsive and attractive inter-species interactions.

In the given illustrations, where we fix the intra-species interaction to be repulsive, we observe that the dominant instability mode determines the number of parts that the homogeneous state breaks down. As shown, for sufficient high interaction, although the total angular momentum remains conserved, the individual vorticity can be lost. In the case of attractive inter-species interactions, we first observe the existence of a stable region, which occurs due to the geometry. Also verified in this attractive case, is the split of the system according to the most unstable mode, before the occurrence of the collapse.

Finally, we understand that the present study can be relevant in order to establish initial parameters for experimental tests and realizations, as well as for more involved theoretical approaches in which the miscibility of different kind of particles can be modified by their specific characteristics. Apart of possible experimental setup difficulties for realizations in microgravity conditions, a perspective theoretical investigation should be to extend the present study to the case of strongly mass-imbalanced mixtures, such as with  $^{87}\text{Rb}$  and  $^{133}\text{Cs}$  [85, 86], which have been explored in cold-atom experiments. In view of previous studies [47], binary systems with strong mass differences are expected to impact on the results we have presented, being of interest to verify how the stability and density distributions are affected. Therefore, by considering coupled systems with identical masses, the immediate possible applications of our analysis could be when considering binary mixtures of the same isotope with different internal spin states, as being considered

in Refs. [16, 17], or in the case of a mixture with two close atomic isotopes, as  $^{85}\text{Rb}$  and  $^{87}\text{Rb}$ , which should present similar results as the ones observed for identical mass mixtures. Another unavoidable future investigation refers to energetic instabilities, expected to emerge in the condensates with quantized vortices in spherical geometry, which can be verified by considering a time-dependent dissipation mechanism related to condensate interactions with the thermal cloud.

### Appendix A: Numerical method for time evolution

The numerical approach to solve Eq. (1) involves a combination of techniques. First, a split-step method is used to separate the evolution of nonlinear and linear parts. Thus, from (1), at an arbitrary instant, we take a function  $\zeta_i \equiv \zeta_i(\theta, \phi, t) = \psi_i$ , which satisfy

$$\frac{\partial}{\partial t} \zeta_i = \left( \sum_k \gamma_{ik} |\psi_k|^2 \right) \zeta_i. \quad (\text{A1})$$

The nonlinear part is propagated in small time steps with direct exponentiation, since both species densities are considered frozen and treated as static potentials.

The linear part demands some care to handle the boundary conditions at the poles. A suitable approach is to work on the Fourier transformed space in the  $\phi$ -direction, which simplifies the Laplacian (2) for each mode in the series. Thus from  $\zeta_i$ , we introduce

$$\zeta_i = \sum_k e^{ik\phi} \tilde{\zeta}_{ik}, \quad (\text{A2})$$

for the given time instant, whereas the Fourier weights  $\tilde{\zeta}_{ik}$  are functions of  $\theta$  and time. Thereafter, from the linear part of Eq. (1) we have the following time-dependent

equation for each mode  $k$

$$\frac{\partial}{\partial t} \tilde{\zeta}_{ik} = -\frac{1}{2} \left[ \frac{1}{\sin \theta} \frac{\partial}{\partial \theta} \left( \sin \theta \frac{\partial}{\partial \theta} \right) - \frac{k^2}{\sin^2 \theta} \right] \tilde{\zeta}_{ik}. \quad (\text{A3})$$

Within this approach, we can now clearly introduce the boundary conditions at the poles, which depend on the frequency mode  $k$  along the  $\phi$  direction as

$$\tilde{\zeta}_{ik} \Big|_{\theta=0,\pi} = \delta_{0,k}, \quad \frac{\partial \tilde{\zeta}_{i0}}{\partial \theta} \Big|_{\theta=0,\pi} = 0. \quad (\text{A4})$$

Once the boundaries are set appropriately, the finite differences Crank-Nicolson semi-implicit method was used to integrate the equations for each mode  $k$  in Eq. (A3). After the solutions are determined for the next step for the coefficients, they are transformed back to the spatial  $\phi$  coordinate.

In summary, the split-step method requires a time step and a discretization grid, then Eq. (A1) is propagated half time step, then the linear part is solved in Eq. (A3) for an entire time step going forward and backward of the Fourier space, and finally, the nonlinear part is propagated by another half time step, with the initial condition taken from the resulting linear part propagation.

### ACKNOWLEDGEMENTS

The authors thank discussion with Profs. E.J.V. Passos and A. F. R. T. Piza. We also acknowledge the Brazilian agencies Fundação de Amparo à Pesquisa do Estado de São Paulo (FAPESP) [Contracts 2018/02737-4 (AA), 2017/05660-0 (LT), 2016/17612-7 (AG)], Conselho Nacional de Desenvolvimento Científico e Tecnológico [Procs. 304469-2019-0(LT) and 306920/2018-2 (AG)] and Coordenação de Aperfeiçoamento de Pessoal de Nível Superior [Proc. 88887.374855/2019-00 (LB)].

- 
- [1] S. N. Bose, Plancks Gesetz und Lichtquantenhypothese, Z. Phys. 26, 178 (1924).
  - [2] A. Einstein, Quantentheorie des einatomigen idealen Gases, Sitz. Ber. Preuss. Akad. Wiss. (Berlin) 1, 3 (1925)
  - [3] M.H. Anderson, J.R. Ensher, M.R. Matthews, C.E. Wieman, and E.A. Cornell, Observation of Bose-Einstein Condensation in a Dilute Atomic Vapor, Science **269**, 198 (1995).
  - [4] K.B. Davis, M.-O. Mewes, M.R. Andrews, N.J. van Druten, D.S. Durfee, D.M. Kurn, and W. Ketterle, Bose-Einstein condensation in a gas of sodium atoms, Phys. Rev. Lett. **75**, 3969 (1995).
  - [5] C. C. Bradley, C. A. Sackett, J. J. Tollett, and R. G. Hulet, Evidence of Bose-Einstein condensation in an atomic gas with attractive interactions, Phys. Rev. Lett. **75**, 1687 (1995).
  - [6] H. Feshbach, Unified theory of nuclear reactions, Ann. Phys. N.Y. **5**, 357 (1958); H. Feshbach, Unified theory of nuclear reactions II, Ann. Phys. N.Y. **19**, 287 (1962).
  - [7] S. Inouye, M. R. Andrews, J. Stenger, H.-J. Miesner, D. M. Stamper-Kurn and W. Ketterle, Observation of Feshbach resonances in a Bose-Einstein condensate, Nature **392**, 151 (1998).
  - [8] E. Timmermans, P. Tommasini, M. Hussein, and A. Kerman, Feshbach resonances in atomic Bose-Einstein condensates, Phys. Rep. **315**, 199 (1999).
  - [9] C. Chin, R. Grimm, P. Julienne, and E. Tiesinga, Feshbach resonances in ultracold gases, Rev. Mod. Phys. **82**, 1225 (2010).
  - [10] F. Dalfovo, S. Giorgini, L. P. Pitaevskii, and S. Stringari, Theory of Bose-Einstein condensation in trapped gases, Rev. Mod. Phys. **71**, 463 (1999).
  - [11] L. P. Pitaevskii and S. Stringari, Bose-Einstein Condensation, Clarendon Press, Oxford, 2003.
  - [12] C. J. Pethick, H. Smith, Bose-Einstein Condensation in Dilute Gases, Cambridge University Press, Cambridge

- UK, 2nd ed. (2008)
- [13] I. Bloch, J. Dalibard, and W. Zwerger, Many-body physics with ultracold gases, *Rev. Mod. Phys.* **80**, 885 (2008).
- [14] A. L. Fetter, Rotating trapped Bose-Einstein condensates, *Rev. Mod. Phys.* **81**, 647 (2009).
- [15] L. Pitaevskii and S. Stringari, *Bose-Einstein Condensation and Superfluidity*, Oxford University Press, Oxford, 2016.
- [16] T. L. Ho and V. B. Shenoy, Binary Mixtures of Bose Condensates of Alkali Atoms, *Phys. Rev. Lett.* **77**, 3276 (1996).
- [17] C. J. Myatt, E. A. Burt, R. W. Ghrist, E. A. Cornell, and C. E. Wieman, Production of Two Overlapping Bose-Einstein Condensates by Sympathetic Cooling, *Phys. Rev. Lett.* **78**, 586 (1997).
- [18] D. S. Hall, M. R. Matthews, J. R. Ensher, C. E. Wieman, and E. A. Cornell, Dynamics of Component Separation in a Binary Mixture of Bose-Einstein Condensates, *Phys. Rev. Lett.* **81**, 1539 (1998).
- [19] C. K. Law, H. Pu, N. P. Bigelow, and J. H. Eberly, "Stability Signature" in Two-Species Dilute Bose-Einstein Condensates, *Phys. Rev. Lett.* **79**, 3105 (1997).
- [20] P. Ao and S.T. Chui, Binary Bose-Einstein Condensate Mixtures in Weakly and Strongly Segregated Phases, *Phys. Rev. A* **58**, 4836 (1998).
- [21] K. Kasamatsu, M. Tsubota, and M. Ueda, Vortex Phase Diagram in Rotating Two-Component Bose-Einstein Condensates, *Phys. Rev. Lett.* **91**, 150406 (2003).
- [22] H. Saito, Y. Kawaguchi, and M. Ueda, Ferrofluidity in a Two-Component Dipolar Bose-Einstein Condensate, *Phys. Rev. Lett.* **102**, 230403 (2009).
- [23] I. Ferrier-Barbut, M. Delehaye, S. Laurent, A. T. Grier, M. Pierce, B. S. Rem, F. Chevy, C. Salomon, A mixture of Bose and Fermi superfluids, *Science* **345**, 1035 (2014). Heteronuclear ultra-cold chemistry as a new field of interest with an intense research activity in recent years:
- [24] J. Ulmanis, S. Häfner, E.D. Kuhnle, M. Weidemüller, Heteronuclear Efimov resonances in ultracold quantum gases, *Natl. Sci. Rev.* **3**, 174 (2016).
- [25] H. Yang, D.-C. Zhang, L. Liu, Y.-X. Liu, J. Nan, B. Zhao, J.-W. Pan, Observation of magnetically tunable Feshbach resonances in ultracold  $^{23}\text{Na}^{40}\text{K}+^{40}\text{K}$  collisions, *Science* **363**, 261 (2019).
- [26] A. Green, H. Li, J. H. S. Toh, X. Tang, K. C. McCormick, M. Li, E. Tiesinga, S. Kotochigova, and S. Gupta, Feshbach resonances in  $p$ -wave three-body recombination within Fermi-Fermi mixtures of open-shell  $^6\text{Li}$  and closed-shell  $^{173}\text{Yb}$  Atoms. *Phys. Rev. X* **10**, 031037 (2020).
- [27] M. A. Shalchi, M. T. Yamashita, T. Frederico, and L. Tomio, Cold atom-dimer reaction rates with  $^4\text{He}$ ,  $^6,^7\text{Li}$  and  $^{23}\text{Na}$ , *Phys. Rev. A* **102**, 062814 (2020).
- [28] L. Wen, W. M. Liu, Y. Cai, J. M. Zhang, and J. Hu, Controlling phase separation of a two-component Bose-Einstein condensate by confinement, *Phys. Rev. A* **85**, 043602 (2012).
- [29] S. Bandyopadhyay, A. Roy, and D. Angom, Dynamics of phase separation in two-species Bose-Einstein condensates with vortices, *Phys. Rev. A* **96**, 043603 (2017).
- [30] S. Jochim, M. Bartenstein, A. Altmeyer, G. Hendl, S. Riedl, C. Chin, J. H. Denschlag, R. Grimm, Bose-Einstein Condensation of Molecules, *Science* **302**, 2101 (2003).
- [31] G. Thalhammer, G. Barontini, L. De Sarlo, J. Catani, F. Minardi, and M. Inguscio, Double Species Bose-Einstein Condensate with Tunable Interspecies Interactions, *Phys. Rev. Lett.* **100**, 210402 (2008).
- [32] A. Trautmann, P. Ilzhöfer, G. Durastante, C. Politi, M. Sohmen, M.J. Mark, and F. Ferlaino, Dipolar quantum mixtures of erbium and dysprosium atoms, *Phys. Rev. Lett.* **121**, 213601 (2018).
- [33] P. Ilzhöfer, G. Durastante, A. Patscheider, A. Trautmann, M.J. Mark, and F. Ferlaino, Two-species five-beam magneto-optical trap for erbium and dysprosium *Phys. Rev. A* **97**, 023633 (2018).
- [34] A. Burchianti, C. D'Errico, M. Prevedelli, L. Salasnich, F. Ancilotto, M. Modugno, F. Minardi, and C. Fort, A Dual-Species Bose-Einstein Condensate with Attractive inter-species Interactions, *Condens. Matter* **5**, 21 (2020).doi:10.3390/condmat5010021.
- [35] A. Richaud, A. Zenesini, V. Penna, The mixing-demixing phase diagram of ultracold heteronuclear mixtures in a ring trimer, *Sci. Rep.* **9**, 6908 (2019).
- [36] K. Góral and L. Santos, Ground state and elementary excitations of single and binary Bose-Einstein condensates of trapped dipolar gases *Phys. Rev. A* **66**, 023613 (2002).
- [37] T. Lahaye, et al., The physics of dipolar bosonic quantum gases, *Rep. Prog. Phys.* **72**, 126401 (2009).
- [38] R. M. Wilson, S. Ronen and J. L. Bohn, Stability and excitations of a dipolar Bose-Einstein condensate with a vortex, *Phys. Rev. A* **79**, 013621 (2009).
- [39] R. N. Bisset and P. B. Blakie, Crystallization of a dilute atomic dipolar condensate, *Phys. Rev. A* **92**, 061603(R) (2015).
- [40] H. Kadau, M. Schmitt, M. Wenzel, C. Wink, T. Maier, I. Ferrier-Barbut, T. Pfau, Observing the Rosensweig instability of a quantum ferrofluid, *Nature* **530**, 194 (2016).
- [41] K.-T. Xi and H. Saito, Droplet formation in a Bose-Einstein condensate with strong dipole-dipole interaction, *Phys. Rev. A* **93**, 011604(R) (2016).
- [42] A. Gammal, T. Frederico, L. Tomio, and P. Chomaz, Liquid-gas phase transition in Bose-Einstein condensates with time evolution, *Phys. Rev. A* **61**, 051602(R) (2000).
- [43] F. K. Abdullaev, A. Gammal, L. Tomio, and T. Frederico, Stability of trapped Bose-Einstein condensates, *Phys. Rev. A* **63**, 043604 (2001).
- [44] R. K. Kumar, P. Muruganandam, L. Tomio, and A. Gammal, Miscibility in coupled dipolar and non-dipolar Bose-Einstein condensates, *J. Phys. Commun.* **1**, 035012 (2017).
- [45] R. K. Kumar, L. Tomio, B. A. Malomed, and A. Gammal, Vortex lattices in binary Bose-Einstein condensates with dipole-dipole interactions, *Phys. Rev. A* **96**, 063624 (2017).
- [46] R. K. Kumar, L. Tomio, and A. Gammal, Vortex patterns in rotating dipolar Bose-Einstein condensate mixtures with squared optical lattices, *J. Phys. B: At. Mol. Opt. Phys.* **52**, 025302 (2019).
- [47] R. K. Kumar, A. Gammal, L. Tomio, Mass-imbalanced Bose-Einstein condensed mixtures in rotating perturbed trap, *Phys. Lett. A* **384**, 126535 (2020).
- [48] R. K. Kumar, L. Tomio, and A. Gammal, Spatial separation of rotating binary Bose-Einstein condensates by tuning the dipolar interactions, *Phys. Rev. A* **99**, 043606 (2019).
- [49] A.-C. Lee, D. Baillie, P. B. Blakie, and R. N. Bisset, Miscibility and stability of dipolar bosonic mixtures, *Phys.*

- Rev. A **103**, 063301 (2021).
- [50] S. Ishino, M. Tsubota, and H. Takeuchi, Counter-rotating vortices in miscible two-component Bose-Einstein condensates, *Phys. Rev. A* **88**, 063617 (2013).
- [51] Z. Chen, Y. Li, N. P. Proukakis and B. A. Malomed, Immiscible and miscible states in binary condensates in the ring geometry, *New J. Phys.* **21**, 073058 (2019).
- [52] E. Nicolau, J. Mompert, B. Juliá-D´az, and V. Ahufinger, Orbital angular momentum dynamics of Bose-Einstein condensates trapped in two stacked rings, *Phys. Rev. A* **102**, 023331 (2020).
- [53] T. Kanai, W. Guo, M. Tsubota, and D. Jin, Torquing the Condensate: Angular Momentum Transport in Bose-Einstein Condensates by Solitonic "Corkscrew", *Phys. Rev. Lett.* **124**, 105302 (2020).
- [54] M. Trippenbach, K. Góral, K. Rzazewski, B. Malomed, and Y. B. Band, Structure of binary Bose-Einstein condensates, *J. Phys. B* **33**, 4017 (2000).
- [55] S. B. Papp, J. M. Pino, and C. E. Wieman, Tunable Miscibility in a Dual-Species Bose-Einstein Condensate, *Phys. Rev. Lett.* **101**, 040402 (2008).
- [56] C. R. Cabrera, L. Tanzi, J. Sanz, B. Naylor, P. Thomas, P. Cheiney, and L. Tarruell, Quantum liquid droplets in a mixture of Bose-Einstein condensates, *Science* **359**, 301 (2018).
- [57] G. Semeghini, G. Ferioli, L. Masi, C. Mazzinghi, L. Wolswijk, F. Minardi, M. Modugno, G. Modugno, M. Inguscio, and M. Fattori, Self-Bound Quantum Droplets of Atomic Mixtures in Free Space, *Phys. Rev. Lett.* **120**, 235301 (2018).
- [58] C. D'Errico, A. Burchianti, M. Prevedelli, L. Salasnich, F. Ancilotto, M. Modugno, F. Minardi, and C. Fort, Observation of quantum droplets in a heteronuclear bosonic mixture, *Phys. Rev. Research* **1**, 033155 (2019).
- [59] O. Zobay and B.M. Garraway, Two-Dimensional Atom Trapping in Field-Induced Adiabatic Potentials, *Phys. Rev. Lett.* **86**, 1195 (2001).
- [60] O. Zobay and B.M. Garraway, Atom trapping and two-dimensional Bose-Einstein condensates in field-induced adiabatic potentials, *Phys. Rev. A* **69** 023605 (2004).
- [61] <https://coldatomlab.jpl.nasa.gov/>, <http://www.sussex.ac.uk/broadcast/read/45233>
- [62] E.R. Elliott, M.C. Krutzik, J.R. Williams, R.J. Thompson, and D.C. Aveline, Nasa's cold atom lab (cal): system development and ground test status, *npj Microgravity* **4**, 1 (2018).
- [63] N. Lundblad, R.A. Carollo, C. Lannert, M.J. Gold, X. Jiang, D. Paseltiner, N. Sergay, and D.C. Aveline, Shell potentials for microgravity Bose-Einstein condensates, *npj Microgravity* **30**, 1 (2019).
- [64] A. Tononi and L. Salasnich, Bose-Einstein Condensation on the Surface of a Sphere, *Phys. Rev. Lett.* **123**, 160403 (2019).
- [65] S. J. Bereta, L. Madeira, V. S. Bagnato and M. A. Caracanhas, Bose-Einstein condensation in spherically symmetric traps, *Am. J. Phys.* **87**, 924 (2019).
- [66] S. Prestipino and P. V. Giaquinta, Ground state of weakly repulsive soft-core bosons on a sphere, *Phys. Rev. A* **99**, 063619 (2019).
- [67] A. Tononi, F. Cinti, and L. Salasnich, Quantum Bubbles in Microgravity, *Phys. Rev. Lett.* **125**, 010402 (2020).
- [68] P. C. Diniz, E. A. B. Oliveira, A. R. P. Lima and E. A. L. Henn, Ground state and collective excitations of a dipolar Bose-Einstein condensate, *Sci. Rep.* **10**, 4831 (2020).
- [69] K. Padavić, Kuei Sun, C. Lannertand, S. Vishveshwara, Vortex-antivortex physics in shell-shaped Bose-Einstein condensates, *Phys. Rev. A* **102**, 043305 (2020).
- [70] D. C. Aveline, et al., Observation of Bose-Einstein condensates in an Earth-orbiting research lab, *Nature* **582**, 193 (2020).
- [71] R. A. Carollo, et al., Observation of ultracold atomic bubbles in orbital microgravity, arXiv:2108.05880v1.
- [72] S. J. Bereta, M. A. Caracanhas, and A. L. Fetter, Superfluid vortex dynamics on a spherical film, *Phys. Rev. A* **103**, 053306 (2021).
- [73] A. Tononi, A. Pelster and L. Salasnich, Topological superfluid transition in bubble-trapped condensates, arXiv:2014.04585v1.
- [74] D. Petrov, Quantum Mechanical Stabilization of a Collapsing Bose-Bose Mixture, *Phys. Rev. Lett.* **115**, 155302 (2015).
- [75] P. Naidon and D. S. Petrov, Mixed Bubbles in Bose-Bose Mixtures, *Phys. Rev. Lett.* **126**, 115301 (2021).
- [76] T. D. Lee, K. Huang, and C. N. Yang, Eigenvalues and Eigenfunctions of a Bose System of Hard Spheres and Its Low-Temperature Properties, *Phys. Rev.* **106**, 1135 (1957).
- [77] T. G. Skov, M. G. Skou, N. B. Jørgensen, and J. J. Arlt, Observation of a Lee-Huang-Yang Fluid, *Phys. Rev. Lett.* **126** 230404 (2021).
- [78] Z.-H. Luo, W. Pang, B. Liu, Y.-Y. Li, B. A. Malomed, A new form of liquid matter: Quantum droplets, *Front. Phys.* **16**, 32201 (2021).
- [79] B. Jackson, N. P. Proukakis, C. F. Barenghi, and E. Zaremba, Finite-temperature vortex dynamics in Bose-Einstein condensates, *Phys. Rev. A* **79**, 053615 (2009).
- [80] M. Kreibich, J. Mainand G. Wunner, Relation between the eigenfrequencies of Bogoliubov excitations of Bose-Einstein condensates and the eigenvalues of the Jacobian in a time-dependent variational approach, *Phys. Rev. A* **86**, 013608 (2012).
- [81] M. Brtko, A. Gammal, and B. Malomed, Hidden vorticity in binary Bose-Einstein condensates, *Phys. Rev. A* **82**, 053610 (2010).
- [82] For details, see [https://en.wikipedia.org/wiki/Stirling's\\_approximation](https://en.wikipedia.org/wiki/Stirling's_approximation)
- [83] J. Yang, Newton-conjugate-gradient methods for solitary wave computations, *J. Comp. Phys.* **228**, 7007 (2009).
- [84] For a movie illustrating the time-evolution of the instability for the attractive case, see Supplemental Material.
- [85] D. J. McCarron, H. W. Cho, D. L. Jenkin, M. P. Köpinger, and S. L. Cornish, Dual-species Bose-Einstein condensate of  $^{87}\text{Rb}$  and  $^{133}\text{Cs}$ , *Phys. Rev. A* **84**, 011603(R) (2011).
- [86] A. D. Lercher, T. Takekoshi, M. Debatin, B. Schuster, R. Rameshan, F. Ferlaino, R. Grimm, and H.-C. Nägerl, Production of a dual-species Bose-Einstein condensate of Rb and Cs atoms, *Eur. Phys. J. D* **65**, 3 (2011).